Hydrothermal Formation of W/Mo-Oxides: A Multidisciplinary Study of Growth and Shape

Ragnar Kiebach,[†] Nicole Pienack,[†] Wolfgang Bensch,[†] Jan-Dierk Grunwaldt,[‡,§] Alexej Michailovski,[‡] Alfons Baiker,[‡] Thomas Fox,[||] Ying Zhou,[||] and Greta R. Patzke*[,||]

Institute of Inorganic Chemistry, University of Kiel, Olshausenstrasse 40, D-24098 Kiel, Germany, Institute for Chemical and Bioengineering, Department of Chemistry and Applied Biosciences, ETH Zurich, Hönggerberg-HCI, CH-8093 Zurich, Switzerland, and Institute of Inorganic Chemistry, University of Zurich, Wintherthurerstrasse 190, CH-8057 Zurich, Switzerland

Received September 28, 2007. Revised Manuscript Received January 30, 2008

The hydrothermal formation of mixed nanoscale W/Mo-oxides with the hexagonal tungsten bronze (HTB) structure has been investigated by in situ EDXRD (energy dispersive X-ray diffraction). Compared to the binary oxide systems, they display intermediate kinetics with a nucleation-controlled mechanism dominated by the slow growing tungsten component. Furthermore, the thermal stability of nanostructured W/Mo-HTB compounds has been monitored through combined in situ X-ray absorption spectroscopy (XAS) and XRD in reducing and oxidizing atmospheres. Their transformation into other mixed nanostructures was only observed above 300 °C in O_2- and H_2-containing atmospheres. In addition, the shape of nanoscale hexagonal W/Mo-oxides can be expanded into a variety of morphologies via the use of alkali chlorides as hydrothermal additives. The alkali cations exert a two-fold role as internal stabilizers and external shape control agents. Their mobility within the channels of the W/Mo-oxide host framework has been investigated by solid state NMR spectroscopy.

1. Introduction

Transition metal oxides (TMOs) play an important role in modern materials chemistry. Their almost unlimited number of structural options is both a blessing and a curse:[1] While the ongoing discovery of new TMO structures continues to bring forward substances with key properties and applications (e.g., superconductors, semiconductors, magnetic materials, or fast ion conductors), it can be extremely difficult to prepare the according TMOs in a predictive manner on a larger scale.[2] This applies especially for downscaling TMO-based materials to nanoscopic dimensions.[3] For this purpose, solvo- and hydrothermal methods are a powerful tool due to their exceptional parameter tuning options that can be adapted and optimized to bring forward a wide spectrum of materials that may be difficult to access with conventional preparative methods, for example, nanoparticles, metastable compounds/ or hybrid materials.[4] However, at the moment, too little is known about the mechanisms occurring under hydrothermal conditions to predict the products resulting from a new experimental setup in a general fashion. Therefore, in situ investigations of hydrothermal reactions are essential to fully explore their potential for morphology control in materials synthesis.[5,6]

In our previous work, we have focused on the investigation of the formation of nanoscale molybdenum[7] and tungsten oxides[8] with in situ XAS (EXAFS, extended X-ray absorption fine structure and XANES, X-ray absorption near-edge structure) and EDXRD (energy dispersive X-ray diffraction) techniques. In addition, we have demonstrated that the nanoscale morphology of hexagonal tungsten bronzes (HTBs) can be adjusted through the use of alkali cations as additives.[8] Furthermore, we have developed a convenient one-step hydrothermal approach to mixed nanostructured W/Mo-oxides starting from readily available precursor materials.[9]

In the present study, these previous analytical and synthetic results are applied on the formation of nanostructured W/Mo-HTBs.[9] Generally, ternary and higher TMOs often benefit from a "synergistic" effect, because the combination of two or more oxides can substantially enhance the properties of

* To whom correspondence should be addressed. Phone: +41 44 63 54691. Fax: +41 44 63 56802. E-mail: greta.patzke@aci.uzh.ch.
[†] University of Kiel.
[‡] ETH Zurich.
[§] Present address: Department of Chemical and Biochemical Engineering, Technical University of Denmark, DK-2800 Kgs. Lyngby, Denmark.
[||] University of Zurich.

(1) Rao, C. N. R.; Raveau, B. *Transition Metal Oxides*, 2nd ed.; Wiley-VCH: New York, 1998.
(2) (a) Rao, C. N. R.; Deepak, F. L.; Gundiah, G.; Govindaraj, A. *Prog. Solid State Chem.* **2005**, *31*, 5. (b) Niederberger, M.; Garnweitner, G.; Pinna, N.; Neri, G. *Prog. Solid State Chem.* **2005**, *33*, 59. (c) Patzke, G. R.; Krumeich, F.; Nesper, R. *Angew. Chem., Int. Ed.* **2003**, *42*, 972.
(3) (a) Mann, S. *Angew. Chem., Int. Ed.* **2000**, *39*, 3392. (b) Wang, T. P.; Antonietti, M.; Cölfen, H. *Chem. Eur. J.* **2006**, *12*, 5722.
(4) (a) Byrappa, K.; Yoshimura, M. Handbook of Hydrothermal Technology; Noyes: Park Ridge, NJ, 2001. (b) Demazeau, G. *J. Mater. Chem.* **1999**, *9*, 15.
(5) Cheetham, A. K.; Mellot, C. F. *Chem. Mater.* **1997**, *9*, 229.
(6) (a) Walton, R. I.; O'Hare, D. *Chem. Commun.* **2000**, 2283. (b) Morris, R. E.; Weigel, S. J.; Norby, P.; Hanson, J. C.; Cheetham, A. K. *J. Synchrotron Radiat.* **1996**, *3*, 301.
(7) (a) Michailovski, A.; Grunwaldt, J.-D.; Baiker, A.; Kiebach, R.; Bensch, W.; Patzke, G. R. *Angew. Chem., Int. Ed.* **2005**, *44*, 5643. (b) Grunwaldt, J.-D.; Ramin, M.; Rohr, M.; Michailovski, A.; Patzke, G. R.; Baiker, A. *Rev. Sci. Instrum.* **2005**, *76*, 054104.
(8) Michailovski, A.; Kiebach, R.; Bensch, W.; Grunwaldt, J. D.; Baiker, A.; Komarneni, S.; Patzke, G. R. *Chem. Mater.* **2007**, *19*, 185.
(9) Michailovski, A.; Krumeich, F.; Patzke, G. R. *Chem. Mater.* **2004**, *16*, 1433.

10.1021/cm7028036 CCC: $40.75 © 2008 American Chemical Society
Published on Web 04/17/2008

Table 1. Recent Developments in the Materials Chemistry of Mixed W/Mo-Oxides

target compound	synthetic pathway	properties/applications	reference
thin MoO_3/WO_3 films	APCVD of metal carbonyls	working electrodes in electrochromic devices	24
mixed W/Mo-oxide films	cathodic electrodeposition from aqueous solutions	enhanced electrochromism and lithium intercalation	25
nanosized mixed W/Mo-oxide thin films	RF-magnetron sputtering	morphology-dependent sensor response towards CO	26,27
MoO_3-WO_3 composites	sintering/calcination methods	humidity sensors/T-dependent surface barriers	28,29
Mo-doped HTBs	hydrothermal methods	immobilization of radio cesium and strontium	30

the binary components. Over the past years, considerable progress has been achieved in the development of catalysts,[10,11] sensors,[12] electrochromic materials,[13] and other applications of mixed W/Mo-oxides (for selected examples cf. Table 1).

In the analytical part of the paper, we characterize the growth process of mixed W/Mo-HTBs with in situ EDXRD methods. Next, the redox chemistry of nanoscale hexagonal W/Mo-oxides is investigated with complementary in situ X-ray diffraction and in situ EXAFS/XANES spectroscopy. X-ray absorption spectroscopic techniques have been proven to be an efficient tool in the synthesis of oxide materials in general,[14] and for the analysis of the detailed structural features of Mo- and W-oxides in particular.[7,15] In this way, the effect of thermal treatment in oxygen- and hydrogen-containing atmospheres on the phase and morphology of the mixed oxide materials was monitored. The resulting information about the stability and the structural transformations of W/Mo-based nanomaterials provides new insights for a more rational synthesis of oxide-based catalysts.[16]

The following synthetic section of the manuscript illustrates the importance of a flexible TMO structural motif for nanoscale morphology control with additive substances.[17,18] Whereas major progress has been achieved in the additive-controlled synthesis of metal nanoparticles,[17] the search for perfect TMO-additive matches is still a major challenge: While organic additives and bio-macromolecules can exert powerful shaping effects in principle,[19] they often decompose at the reaction temperatures required for hydrothermal oxide formation. Secondly, many additives alter the target TMO structure through unwanted side reactions. However, the hexagonal channels of the HTB structure are stabilized through the intercalation of alkali cations,[20] and this turns the reaction between TMO and additive into a specific preparative asset to generate W/Mo-oxide materials with a wide spectrum of morphologies. Generally, the HTB framework easily undergoes redox and diffusion processes: On the one hand, oxygen atoms can diffuse in and out of the tunnels via complex pathways.[20] Furthermore, there is also a delicate interplay between the degree of occupation of the hexagonal tunnels, for example, by alkali cations, and according vacancies in the W sublattice.[20] The mobility of Li^+, Na^+, and Cs^+ in the channel systems of the W/Mo-HTB structure was investigated in terms of solid state NMR spectroscopy. Recently, composite materials of W/Mo-HTBs and polyacrylonitrile have attracted considerable interest for the immobilization of radioactive Sr^{2+} and Cs^+, and ^{133}Cs MAS NMR spectroscopy revealed the presence of different Cs species in the saturated samples.[21] However, the incorporation of alkali cations into the HTB channels has seldom been studied in terms of NMR spectroscopy, because the majority of the investigations have been focused on other tungsten oxide systems.[22,23]

To the best of our knowledge, only very few detailed studies were reported applying a combination of advanced in situ techniques as well as ex situ characterization on the hydrothermal synthesis and nanoscale morphochemistry of mixed W/Mo-oxides. We have chosen this model system to investigate whether hydrothermal synthetic guidelines can be transferred from binary to ternary TMO systems. In the long term, we aim for general strategies for the controlled design of oxide materials. For this purpose, we work towards a systematic hydrothermal "toolbox" approach to TMO nanomaterials that is based on mechanistic insights.

2. Experimental Procedures

2.1. Hydrothermal Experiments. The mixed W/Mo-oxide materials were prepared according to standard hydrothermal

(10) Mestl, G. *J. Raman Spectrosc.* **2002**, *33*, 333.
(11) Ovsitser, O.; Uchida, Y.; Mestl, G.; Weinberg, G.; Blume, A.; Jäger, J.; Dieterle, M.; Hibst, H.; Schlögl, R. *J. Mol. Catal. A* **2002**, *185*, 291.
(12) Prasad, A. K.; Gouma, P. I. *J. Mater. Sci.* **2003**, *38*, 4347.
(13) Ivanova, T.; Gesheva, K. A.; Popkirov, G.; Ganchev, M.; Tzvetkova, E. *Mater. Sci. Eng. B* **2005**, *119*, 232.
(14) (a) Beale, A. M.; Reilly, L. M.; Gopinathan, S. *Appl. Catal. A* **2007**, *325*, 290. (b) Huwe, H.; Fröba, M. *Carbon* **2007**, *45*, 304. (c) Opre, Z.; Grunwaldt, J.-D.; Mallat, T.; Baiker, A. *J. Mol. Catal. A* **2005**, *242*, 224.
(15) (a) Schlögl, R.; Knop-Gericke, A.; Hävecker, M.; Wild, U.; Frickel, D.; Ressler, T.; Jentoft, R. E.; Wienold, J.; Mestl, G.; Blume, A.; Timpe, O.; Uchida, Y. *Top. Catal.* **2001**, *15*, 219. (b) Purans, J.; Kuzmin, A.; Parent, P.; Laffon, C. *Electrochim. Acta* **2001**, *46*, 1973.
(16) Giebeler, L.; Kampe, P.; Wirth, A.; Adams, A. H.; Kunert, J.; Fuess, H.; Vogel, H. *J. Mol. Catal. A* **2006**, *259*, 309.
(17) Pileni, M. P. *J. Phys. Chem. C* **2007**, *111*, 9019.
(18) Rajam, S.; Mann, S. *J. Chem. Soc., Chem. Commun.* **1990**, 1789.
(19) (a) Komarneni, S.; Gao, F.; Lu, Q. Y. *Langmuir* **2005**, *21*, 6002. (b) Welzel, T.; Meyer-Zaika, W.; Epple, M. *Chem. Commun.* **2004**, 1204.
(20) (a) Guo, J. D.; Reis, K. P.; Whittingham, M. S. *Solid State Ionics* **1992**, *53−56*, 305. (b) Reis, K. P.; Prince, E.; Whittingham, M. S. *Chem. Mater.* **1992**, *4*, 307. (c) Tsuyumoto, I.; Kishimoto, A.; Kudo, T. *Solid State Ionics* **1993**, *59*, 211.
(21) Griffith, C. S.; Sebesta, F.; Hanna, J. V.; Yee, P.; Drabarek, E.; Smith, M. E.; Luca, V. *J. Nucl. Mater.* **2006**, *358*, 151.
(22) (a) Whittle, K. R.; Lumpkin, G. R.; Ashbrook, S. E. *J. Solid State Chem.* **2006**, *179*, 512. (b) Dubson, M. A.; Holcomb, D. F. *Phys. Rev. B* **1986**, *34*, 25.
(23) Xia, Y.; Machida, N.; Wu, X.; Lakeman, C.; van Wüllen, L.; Lange, F.; Levi, C.; Eckert, H. *J. Phys. Chem. B* **1997**, *101*, 9180.
(24) Gesheva, K. A.; Ivanova, T. *Chem. Vap. Deposition* **2006**, *12*, 231.
(25) Kondrachova, L.; Hahn, B. P.; Vijayaraghavan, G.; Williams, R. D.; Stevenson, K. J. *Langmuir* **2006**, *22*, 10490.
(26) Vomiero, A.; Della Mea, G.; Ferroni, M.; Martinelli, G.; Roncarati, G.; Guidi, V.; Comini, E.; Sberveglieri, G. *Mat. Sci. Eng. B* **2003**, *101*, 216.
(27) Morandi, S.; Ghiotti, G.; Chiorino, A.; Bonelli, B.; Comini, E.; Sberveglieri, G. *Sens. Actuators, B* **2005**, *111−112*, 28.
(28) Pokhrel, S.; Nagaraja, K. S. *Phys. Status Solidi* **2003**, *2*, 343.
(29) Malagù, C.; Carotta, M. C.; Morandi, S.; Gherardi, S.; Ghiotti, G.; Giberti, A.; Martinelli, G. *Sens. Actuators, B* **2006**, *118*, 94.

procedures. For experiments with a M:W/Mo-ratio of 60:1, 40 mg (0.13 mmol of W) of $(NH_4)_6[H_2W_{12}O_{40}]\cdot\sim 3H_2O$ (ammonium metatungstate, in the following: AMT), 20 mg of $MoO_3\cdot 2H_2O$ (0.11 mmol of Mo), 10 mL of 25 vol % acetic acid (HAc), and 15 mmol of MCl (M = Li−Cs) were added to a Teflon-lined stainless-steel autoclave with a capacity of 23 mL. The autoclave was then sealed, heated for 2 days at 180 °C, and subsequently cooled to room temperature. The resulting precipitate was collected by filtration, washed with distilled H_2O, EtOH, and acetone, and dried in air. Experiments with a lower M:W/Mo-ratio of 2.5:1 started from 148 mg of AMT (0.60 mmol of W), 58 mg of $MoO_3\cdot 2H_2O$ (0.32 mmol of Mo), 2 mL of 25 vol % HAc, and 2 mmol of MCl (M = Li−Cs), following the above-mentioned hydrothermal routine.

2.2. Analytical Methods. X-ray powder diffraction analyses were conducted on a STOE STADI-P2 diffractometer in transmission mode (flat sample holders, Ge monochromated Cu $K\alpha_1$ radiation) equipped with a position-sensitive detector (resolution ca. 0.01° in 2θ).

For scanning electron microscopy (SEM), performed on a LEO 1530 (FEG) microscope with 1 keV electrons, samples were dispersed in ethanol and subsequently deposited on a silicon wafer. A CamScan CS-44 electron microscope with an EDAX-Phoenix energy-dispersive X-ray spectrometer (EDXS) was employed for approximate elemental analyses. The scanning transmission electron microscopy (STEM) images were recorded on a Philips Tecnai 30F microscope, operated at 300 kV (field emission cathode). In the STEM mode, the electron beam was placed on a selected spot, and an elemental analysis by energy-dispersive X-ray spectroscopy (EDS, EDAX detector) was performed there. Elemental analyses were conducted on a Leco CHN(S)-932 instrument.

2.3. In Situ EDXRD Experiments. All in situ EDXRD experiments were performed at HASYLAB Beamline F3, which receives white synchrotron radiation from a bending magnet with a critical energy of 16 keV and gives a positron beam energy of 4.5 GeV. An energy range from 13.5 to 65 keV can be observed with a maximum at about 20 keV. The diffracted beam is monitored by a nitrogen cooled solid state germanium detector. The detector angle was chosen so that all important Bragg reflections can be detected. The *d*-spacing range is given by $E = 6.199/(d \sin \theta)$. With a detector angle of approximately 3° the observable *d*-spacing range is 2.9 Å to 13.8 Å. The energy resolution $\Delta d/d$ is about 10^{-2} above 26 keV. The beam was collimated to 0.1 mm giving the best results. More experimental details can be found in refs 31 and 32. For the in situ investigations autoclaves with glass liners with an internal diameter of 10 mm and a volume of 10 mL were used. A typical experiment (ratio Mo:W = 1:1) was performed by using 298 mg of $(NH_4)_6[H_2W_{12}O_{40}]\cdot\sim 3H_2O$ (AMT), 144 mg $MoO_3\cdot 2H_2O$, and 1.5 mL 25% HAc as reactants.

2.4. In Situ XRD and EXAFS Experiments. XANES and EXAFS (X-ray absorption near edge structure) and EXAFS data were collected at the Norwegian-Swiss Beamline (SNBL, BM01B) of the European Synchrotron Radiation Facility, ESRF, Grenoble, France. The electron energy is typically 6.0 GeV and the ring current was between 150 and 200 mA. A Si(111) crystal was used as channel-cut monochromator. Harmonic rejection was performed by a double-bounce gold coated mirror system. EXAFS data were collected in transmission mode at room temperature and at elevated temperatures. Three ionization chambers were used for detecting the incoming *I*(0), the transmitted *I*(t), and the through the reference

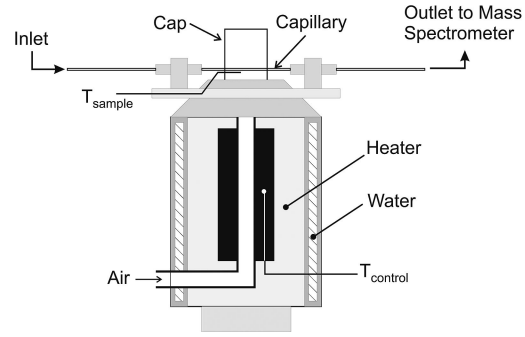

Figure 1. Schematic view of the in situ cell used in the present combined EXAFS/XRD studies.

transmitted *I*(ref), X-rays. Spectra were taken around the Mo K-edge (20.000 keV), using a Mo foil as a reference. They were taken in the energy range of 19.850 to 21.000 keV. The raw data were energy-calibrated, background corrected, and normalized using the WINXAS 3.0 software.[33]

The XRD data were collected at a wavelength $\lambda = 0.5$ Å using a Si(111) double-crystal as monochromator and a two-circle diffractometer equipped with six counting chains (a Si-111 analyzer crystal is mounted in front of each detector, Na−I scintillation counter) and an intrinsic resolution (FWHM) of approximately 0.01°. The spectra were taken using a specially designed and home-built (Figure 1, cf. ref 34) in situ cell, which consists of a sample holder with quartz capillary, a gas blower for heating of the system, a gas supply, and a mass spectrometer for on-line gas analysis. The sample was loaded in the glass microreactor (quartz capillary, Markröhrchen, Hilgenberg GmbH) between two glass wool plugs of 1.0 mm diameter as already described by Clausen et al.[35] The capillary is heated by a hot gas stream (here air, 300−400 L/h) with a commercially available gas blower (Cyberstar S.A., France, 220 V, 1000 W, provided by SNBL). The maximum temperature is 1000 °C. The temperature of the heater ($T_{control}$) was measured by a thermocouple at the heating element in order to control a constant temperature ramp. The actual sample temperature (T_{sample}) was monitored just below the sample. The heater is embedded in ceramics, and the outer side of the oven could be cooled by water or air in order to prevent the surroundings from warming up (e.g., important for ionization chambers). The capillary was enclosed in a Kapton cap around the in situ cell just above the heater where the hot stream of air passed out of the oven to improve the temperature homogeneity.

Typically a flow of 20 mL/min was fed over the catalysts using mass flow controllers (Brooks). Usually, pre-mixed gasses (oxidation in 20% O_2/He, reduction in 5% H_2/He) were utilized. The whole assembly (in situ cell, heater) was mounted on a small *x*,*z*-table (x = translation, z = height) to align the sample in the X-ray beam.

2.5. Solid State NMR Spectroscopy. The NMR spectra were recorded at room temperature on a Bruker DRX-500-spectrometer, which has been modified for solid state capability with MAS sample spinning up to 15 kHz (4 mm rotors) and high power ^{1}H decoupling. The NMR frequencies were 194.41 MHz for ^{7}Li (I = 3/2, QM = 0.045), 132.32 MHz for ^{23}Na (I = 3/2, QM = 0.12), 163.61 MHz for ^{87}Rb (I = 3/2, QM = 0.12), and 65.61 MHz for ^{133}Cs (I = 7/2, QM = 0.003).

(30) Luca, V.; Griffith, C. S.; Drabarek, E.; Chronis, H. *J. Nucl. Mater.* **2006**, *358*, 139.
(31) (a) Avrami, M. *J. Chem. Phys.* **1939**, *7*, 1103. (b) Avrami, M. *J. Chem. Phys.* **1940**, *8*, 212. (c) Avrami, M. *J. Chem. Phys.* **1941**, *9*, 177.
(32) Engelke, L.; Schaefer, M.; Schur, M.; Bensch, W. *Chem. Mater.* **2001**, *13*, 1383.
(33) Ressler, T. *J. Synchrotron Radiat.* **1998**, *5*, 118.
(34) (a) Grunwaldt, J. D.; Caravati, M.; Hannemann, S.; Baiker, A. *Phys. Chem. Chem. Phys.* **2004**, *6*, 3037. (b) Grunwaldt, J.-D.; van Vegten, N.; Baiker, A. *Chem. Commun.* **2007**, 4635.
(35) Clausen, B.S.; Gråbæk, G.; Steffensen, G.; Hansen, P. L.; Topsøe, H. *Catal. Lett.* **1993**, *20*, 23.

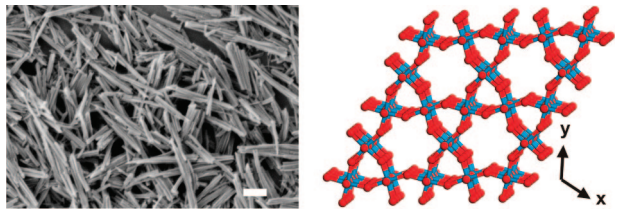

Figure 2. Representative image of W/Mo-oxide rods (left; scale bar = 200 nm) and the tunnel motif of the HTB structure (right).

3. Experimental Results

3.1. Hydrothermal Formation of Nanostructured W/Mo-Oxides. The direct hydrothermal reaction of ammonium metatungstate (AMT, $(NH_4)_6[H_2W_{12}O_{40}]\cdot\sim 3H_2O$) with $MoO_3\cdot 2H_2O$ in acetic acid at 180 °C affords anisotropic $(NH_4)_x(W,Mo)O_3$ particles after 2 days (Figure 2, left).[9] In this procedure, the starting materials are directly transferred into the autoclave without any further pre-treatment. To investigate the influence of homogeneous precursor solutions on the morphology of the product and on the nucleation process, the synthetic protocol was modified as follows: First, clear acidified solutions of AMT and ammonium heptamolybdate ($(NH_4)_6Mo_7O_{24}\cdot 4H_2O$), respectively, were prepared. These solutions were then transferred into the autoclave in the according ratios, and in a series of hydrothermal experiments (180 °C, 2 d) the molar W/Mo-ratio was increased in steps of 10% (metal% in the starting material). In the range between 0% and 60% W, mixtures of microcrystalline starting materials and anisotropic $(NH_4)_x(W,Mo)O_3$ with the HTB structural motif are obtained (Figure 2, right). At higher W/Mo-ratios, the W/Mo-HTBs are exclusively formed, and the smallest rods display diameters in the range of 20−30 nm and lengths around 100 nm. Although the use of homogeneous starting materials might suggest the opposite trend, the nanoparticles obtained from this approach exhibit a stronger tendency towards agglomeration than those formed from the direct reaction of $MoO_3\cdot 2H_2O$ with AMT with no further pre-treatment. Therefore, the one-step pathway starting from AMT and $MoO_3\cdot 2H_2O$ was selected for the following morphological and mechanistic studies.

3.2. Time-Dependent Conversion of AMT and $MoO_3\cdot 2H_2O$ into Nanostructured $(NH_4)_x(W,Mo)O_3$: In Situ EDXRD Investigations. In our previous studies, we have performed kinetic and mechanistic studies on the growth of MoO_3 nanorods[7] and nanostructured HTB tungstates.[8] As these reactions display different results, a kinetic analysis of the mixed W/Mo system provides an excellent opportunity to investigate the parameters which are the decisive factors for the different reaction types and therewith a possible control of the morphology and structure of the product. In situ EDXRD using synchrotron radiation has proven to be an especially powerful method for studying the kinetics of crystallization processes and evaluating their mechanisms.[31,32] The direct monitoring of synthetic processes is superior to ex situ observations, because it permits the collection of much more data with no quenching steps involved. Here, in situ EDXRD measurements are employed to investigate the influence of two main parameters, firstly the influence of the reaction temperature (170−90 °C) and secondly the ratio

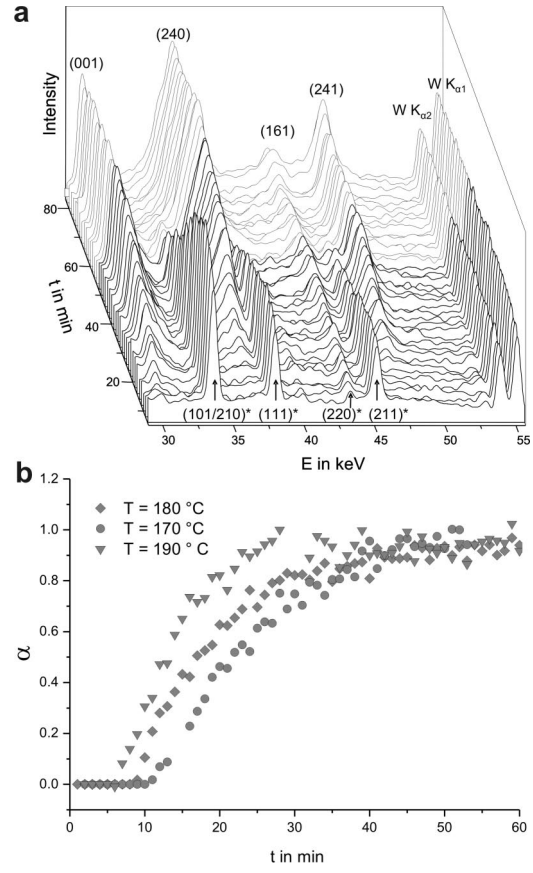

Figure 3. (a) Time-resolved energy-dispersive X-ray powder diffraction pattern of $(NH_4)_x(W,Mo)O_3$ nanorod formation. The indices of the most intense lines of the intermediate and the product phase and W Kα and Kβ fluorescence lines are marked. (b) Extent of reaction α versus time for the formation of $(NH_4)_x(W,Mo)O_3$ rods at different temperatures.

of the educts (W:Mo = 1:3, 1:1, 3:1). In the energy range chosen several reflections of the product and the W resonances (immediately visible) are monitored simultaneously, and the sequence of time resolved spectra is shown in Figure 3a. In all experiments no reflections of the reactants were observed, indicating a very fast dissolution of the W and the Mo sources. Interestingly, for W:Mo ratios < 1 the first observed reflections (Figure 3a) point to the formation of a hexagonal intermediate phase with the structural motif of $(NH_4)_{0.94}H_{3.3}Mo_{5.3}O_{18}$.[36] The growth of this Mo-rich intermediate is finished within 2 min so that a kinetic evaluation of this phase is not possible due its rapid formation. After an induction time, t_{ind}, the product peaks of $(NH_4)_x(W,Mo)O_3$ start to grow. As expected, an increase of the reaction temperature leads in all cases to a decrease of the induction time (range: 10 min (190 °C)−23 min (170 °C)) and overall reaction time (range: 55 min (190 °C)−105 min (170 °C); Figures 3 and 4) and to a faster dissolution of the intermediate.

The integrated intensities of the product and intermediate reflections were normalized against the intensity of the most intense W Kα resonance. Quantitative analysis of the growth rates shows identical behavior for different reflections and confirms an isotropic crystallite growth for both phases. The

(36) Guo, J. D.; Zavalij, P.; Whittingham, M. S. *J. Solid State Chem.* **1995**, *117*, 323.
(37) Kiebach, R.; Pienack, N.; Ordolff, M. E.; Studt, F.; Bensch, W. *Chem. Mater.* **2006**, *18*, 1196.

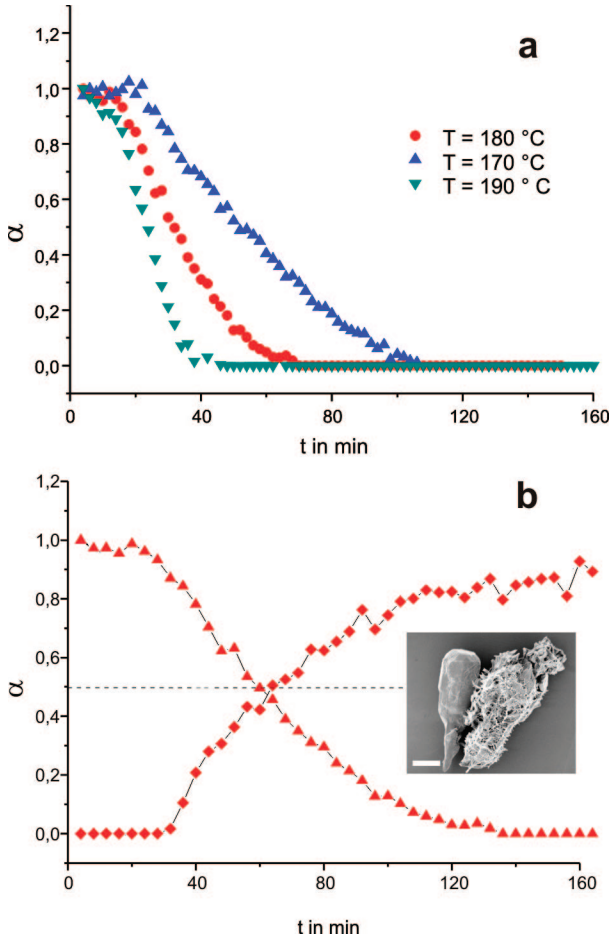

Figure 4. Temperature-dependent dissolution of the AMT starting material (a) and the correlation between the dissolution of AMT and the formation of the product at 170 °C together with a SEM image (inset, scale bar = 2 μm) illustrating the nucleation-controlled formation process of $(NH_4)_x$-$(W,Mo)O_3$ rods (b).

plots of the extent of reaction α (ratio of the normalized intensity at the reaction time t by the intensity at the time t_∞) against the reaction time t (Figures 3 and 4) demonstrate that the induction time t_{ind} depends not only on the reaction temperature but for low W concentration also on the ratio of the educts. The general trend in these cases is that higher induction and longer reaction times are found for increasing W amounts. As presented in Figure 4b, the dissolution of the intermediate and the formation of the product seem to be strongly correlated: Starting from an initial W:Mo ratio of 1:1, the curves of the extent of the reaction for product dissolution and intermediate formation meet for all investigated reaction temperatures exactly at α = 0.5. This highly interesting observation suggests a direct transformation of the intermediate to the final product via a solid−solid transformation. But one can also imagine that the intermediate is dissolved/becomes amorphous and the product crystallization occurs promptly which cannot be resolved within the time resolution of the experiment. For experiments where the Mo content is increased to a ratio of W:Mo = 1:3, only 20% of the intermediate dissolves (not depictured) and the final product contains both phases.

Another interesting feature is the large FWHM of the reflections of the $(NH_4)_x(W,Mo)O_3$ product, which is four times larger than the one of the intermediate compound that

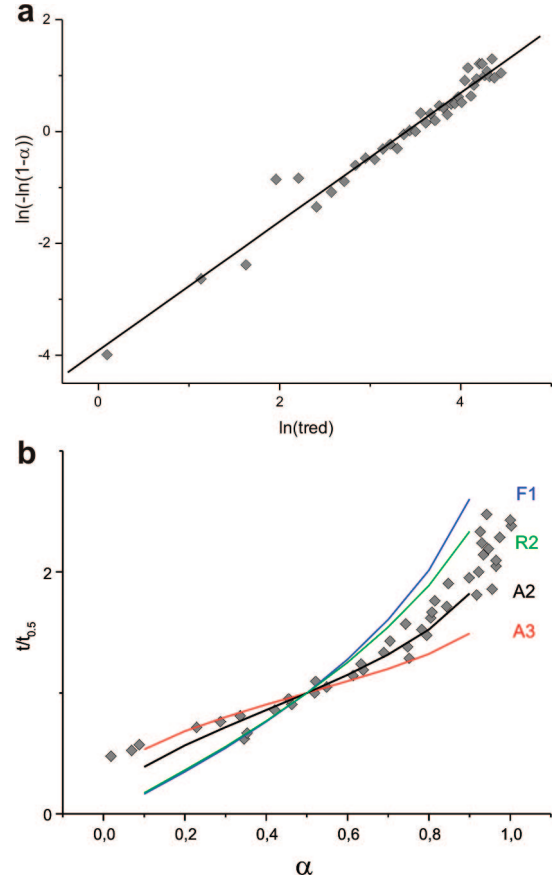

Figure 5. (a) Sharp−Hancock plot and (b) comparison of the evolution of experimental $t/t_{0.5}$ data as a function of α (gray squares) with different theoretical models.

is isostructural with $(NH_4)_{0.94}H_{3.3}Mo_{5.3}O_{18}$. Thus, the size of the monitored crystalline phase can be considered as nanosized material, a result which is in line with the SEM measurements (cf. Figure 2).

The kinetic evaluation of the formation of $(NH_4)_x$-$(W,Mo)O_3$ rods was performed after subtracting the induction time t_0 from time t. When $\ln[-\ln(1-\alpha)]$ versus $\ln(t)$ is plotted (the so-called Sharp−Hancock plot, abbreviated SH) a straight line is obtained for that part of the reaction which follows the same mechanism.[31] A change in the mechanism during the reaction leads to a change in the slope of the curve.

During the formation of $(NH_4)_x(W,Mo)O_3$ rods, no change of the reaction mechanism could be observed over the entire range of experiments, and the experimental points are on a straight line over the whole reaction. A representative example is shown for the reaction at 170 °C in Figure 5a (W/Mo = 1:1). Also the slope of SH plot, from which the reaction exponent can be calculated, is comparable for the entire range of experiments. The values found for the reaction exponent are in the same range of the one published for the W system. For further discussion and an overview about the different models compare refs 8 and 37.

A more detailed analysis is available comparing different established models with the experimental data.[31] The most appropriate model is selected by plotting the experimental $t/t_{0.5}$ data ($t_{0.5}$ is the reaction time at α = 0.5) versus α. This procedure permits a direct comparison

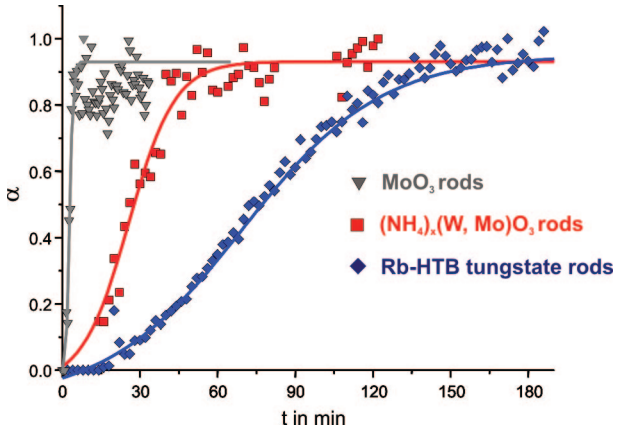

Figure 6. Extent of reaction α versus time for the growth of MoO_3 rods, $(NH_4)_x(W,Mo)O_3$ rods and nanostructured Rb-HTB tungstates.

with different models under consideration. The experimental data fit best with the two-dimensional growth of nuclei (model A2), and this result is in line with the above-mentioned SH plot (Figure 5). At the very early stages of the reaction up to about $\alpha \approx 0.4$ the curve fits well with the three-dimensional growth of nuclei (A3) which can be also rationalized. First small 3D particles are formed (A3) which then exhibit a preferred 2D growth (A2), in accordance with the anisotropic morphology of the materials (see Figure 2). Indeed the kinetic data should be interpreted with some care because several strict conditions have to be fulfilled before the Johnson−Mehl−Avrami kinetics will hold. Nevertheless, the analysis presented above is on a solid scientific ground because important requirements like random nucleation and no hard impingement can be safely assumed. Especially the latter event leads to significant deviations from JMA kinetics. The results are in line with experiments performed under static conditions, because they often display crystals of the starting material with up-grown fibers (cf. inlet Figure 4b). The growth curves for the hydrothermal formation of MoO_3 rods, nanostructured $(NH_4)_x(W,Mo)O_3$, and Rb-HTB rods as a representative example are compared in Figure 6. Whereas the formation of MoO_3 fibers proceeds quantitatively within several minutes via a quick dissolution−precipitation sequence, the nucleation-controlled growth of nanostructured alkali HTBs takes between 2 and 5 h to completion, depending on the cation involved. Consequently, the $(NH_4)_x(W,Mo)O_3$ rods are formed through nucleation control, thereby following the rate-determining consumption step of the tungstate material. In terms of reaction time, they exhibit intermediate kinetics so that the reaction is finished after approximately 1 h.

3.3. Oxidation/Reduction of Nanostructured W/Mo-Oxides: In Situ XRD and EXAFS. *3.3.1. Thermal Treatment in O_2/He Atmosphere.* A representative sample of nanostructured oxide with the composition $(NH_4)_{0.22}(W_{0.43}Mo_{0.57})O_3$ (containing 50 wt % BN) was subjected to thermal treatment in an atmosphere of 20% O_2 in He at a heating rate of 5 °C min^{-1}. During the oxidation, in situ XRD data were taken (Figure 7a) and complemented by EXAFS measurements at selected temperatures (RT, 250 °C, 500 °C). From room temperature to 390 °C, the HTB-structural motif

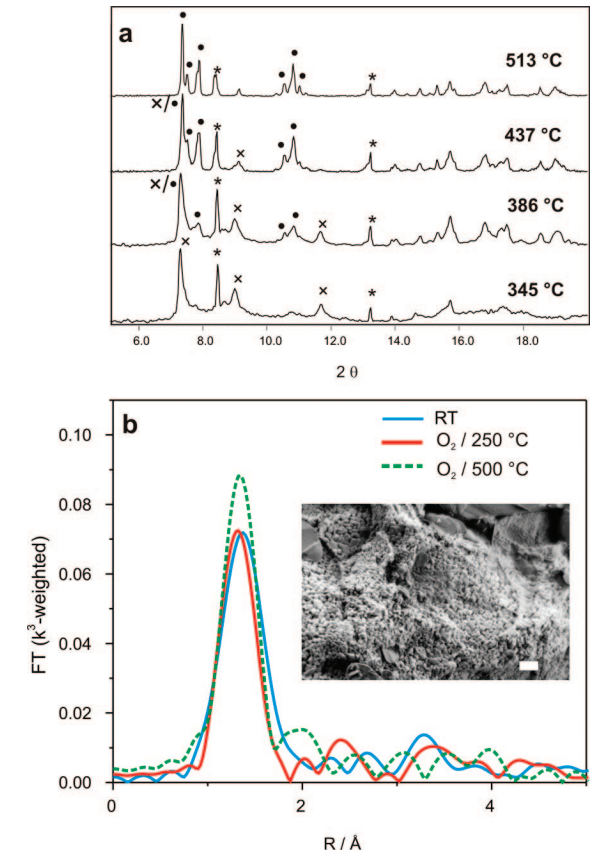

Figure 7. (a) In situ XRD monitoring of the treatment of nanostructured $(NH_4)_{0.22}(W_{0.43}Mo_{0.57})O_3$ (containing 50 wt % BN) in oxygen atmosphere (λ = 0.5 Å, key reflections: * = BN, × = HTB-phase, ● = monoclinic W/Mo-oxide). (b) In situ EXAFS spectra at the Mo K-edge (Fourier transformed) during the treatment of nanostructured $(NH_4)_{0.22}(W_{0.43}Mo_{0.57})O_3$ in oxygen atmosphere together with a representative SEM image of the resulting product (inset, scale bar = 500 nm).

experiences a slight broadening of the reflections and changes in their relative intensities. Whereas the intensity of the (001) and (110) reflections increases, the reflections (101) and (200) become less intense. In the temperature range between 390 and 510 °C, the HTB structure is gradually transformed into a mixed oxide that displays close resemblance to monoclinic WO_3 with a distorted ReO_3 motif (JCPDS No. 43-1305). The key XRD patterns illustrating the temperature-dependent transformation are displayed in Figure 7a.

These structural changes are reflected in the Fourier transformed EXAFS data (Figure 7b): The data suggest an onset of structural changes can be observed at 500 °C, but only small changes of the local structure at the Mo absorber atom occur at 250 °C, also supported by XANES data (cf. ESI). The obtained mixed monoclinic W/Mo-oxide still exhibits nanostructures in the range of 100 nm (cf. inset in Figure 7b). During the oxidation process, the W/Mo-ratio increased from 0.75 to 1 according to EDX analyses of the product. Given that the experimental error of the EDX method is about 3 atom %, this points to a very small loss of molybdenum.

3.3.2. Thermal Treatment in H_2/He Atmosphere. A sample of $(NH_4)_{0.22}(W_{0.43}Mo_{0.57})O_3$ (50 wt % BN) was heated in an atmosphere of 7 vol % H_2 in Ar. In the temperature range

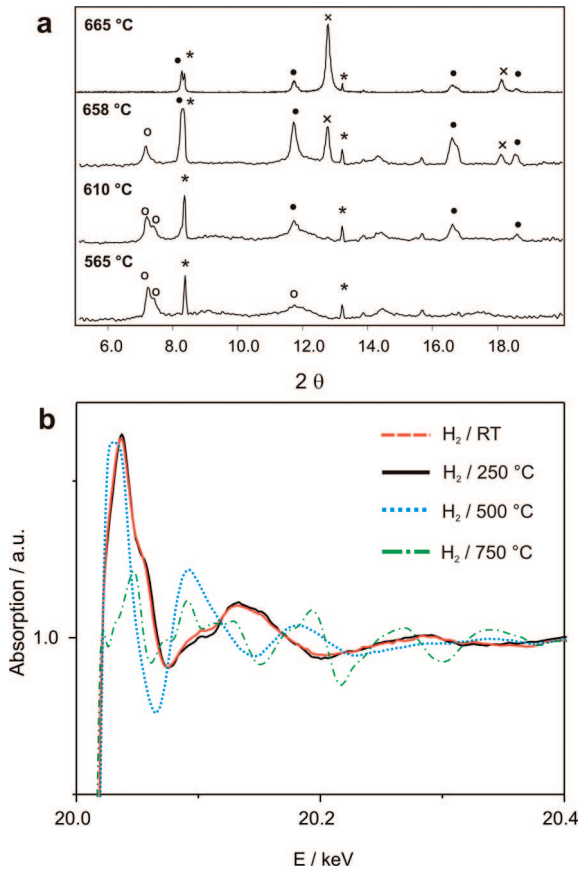

Figure 8. (a) In situ XRD monitoring of the treatment of $(NH_4)_{0.22}(W_{0.43}Mo_{0.57})O_3$ (containing 50 wt % BN) in a hydrogen atmosphere (λ = 0.5 Å, key reflections: * = BN, ○ = HTB structure, ● = WO_2-based motif, × = Mo−W alloy with W-structure). (b) In situ XANES spectra at the Mo K-edge during treatment of $(NH_4)_{0.22}(W_{0.43}Mo_{0.57})O_3$ (containing 50 wt % BN) in 5% H_2/He atmosphere.

between 295 and 500 °C, both in situ XRD and XANES/EXAFS measurements at the Mo K-edge indicate only minor structural alterations (cf. Figure 8).

Note, however, that at 500 °C the near edge structure of the Mo K-edge already changed significantly, also indicated by the Fourier transformed EXAFS data (cf. ESI). Above 500 °C, the reduction to a metallic compound sets in that is structurally related to tungsten (JCPDS No. 4-806). In parallel, a mixed dioxide intermediate is formed that displays a WO_2-based structural motif (JCPDS No. 2-414). After heating to 700 °C, the entire sample is transformed into a mixed metal with a W/Mo ratio of 1 that is isostructural with metallic W (Figure 9). The formation of a metallic Mo−W alloy is also supported by both the XANES (Figure 8b) and EXAFS data. This Mo−W alloy shows a nanostructured morphology consisting of agglomerated particles with diameters of 50 nm and below (cf. inset in Figure 9).

3.4. Influence of Alkali Halides on the Morphology of Nanostructured W/Mo-Oxides. *3.4.1. Reaction of AMT/$MoO_3 \cdot 2H_2O$ Systems in the Presence of MCl.* To investigate the effect of alkali chlorides on the morphology of nanostructured hexagonal W/Mo-oxides, an excess of MCl (M = Li−Cs) was added to the AMT/$MoO_3 \cdot 2H_2O$ hydrothermal system at 180 °C for 2 d of reaction time (M/(W/Mo) = 60:1). As shown in Figure 10, the different alkali chlorides bring forward a wide spectrum of morphologies. The general trends among the mixed W/Mo-alkali oxides (cf. Tables S2 and S3, Supporting Information) can be compared to those observed among the binary hexagonal alkali tungstates:[8] whereas LiCl and NaCl favor the decomposition of microscale intermediates into fibrous products (Figure 10a,b), RbCl and CsCl induce a hierarchical nanostructuring on three levels that leads to the formation of complex spherical aggregates (Figures 10 and 11).

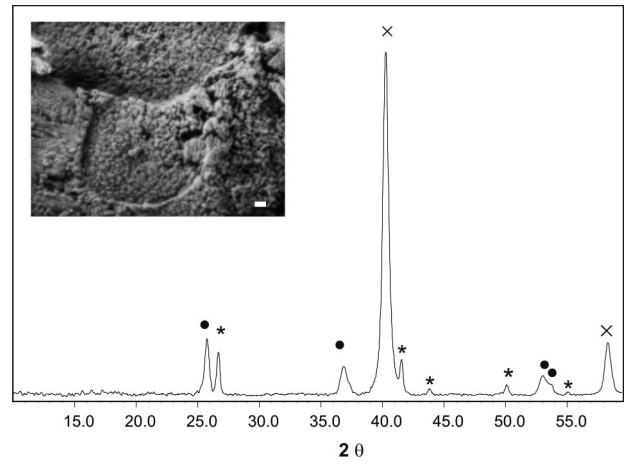

Figure 9. XRD pattern and a representative SEM image (inset, scale bar = 100 nm) of the product obtained after treatment of $(NH_4)_{0.22}(W_{0.43}Mo_{0.57})O_3$ (containing 50 wt % BN) in 5% H_2/He atmosphere (key reflections: * = BN, ● = WO_2-based motif, × = Mo−W-alloy with W-structure).

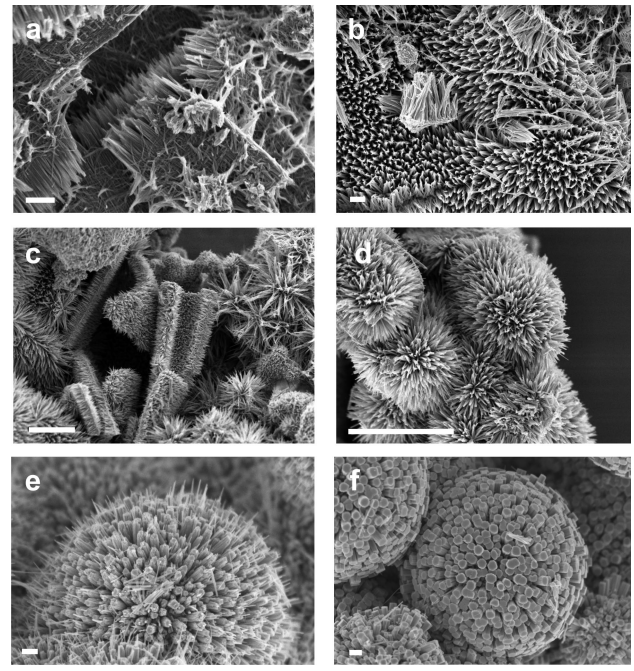

Figure 10. Representative SEM images of nanostructured (a) Li-W/Mo-HTB oxides, (b) Na-W/Mo-HTB oxides, nanostructured K-W/Mo-HTB oxides (c,d) and hierarchically grown Rb-W/Mo-HTB oxides (e,f) obtained from high initial M:W/Mo ratios (60:1); scale bar = 200 nm.

When the hydrothermal reaction is performed with RbCl, very small nanorods (ca. 20 nm in diameter) are organized into cylindrical bundles with diameters around 100 nm (Figure 10e,f). These nanorods assemble into regular spherical aggregates, and their shape can be further altered applying CsCl (Figure 11). In the presence of KCl, a transition from fibrous growth to the organization into flower-like patterns

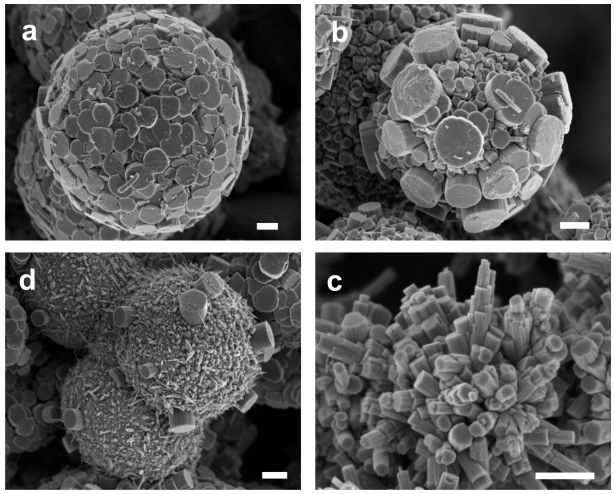

Figure 11. (a−d) Representative SEM images of nanostructured Cs-W/Mo oxides displaying spherical growth patterns (scale bar = 200 nm, M:W/Mo-ratio = 60:1).

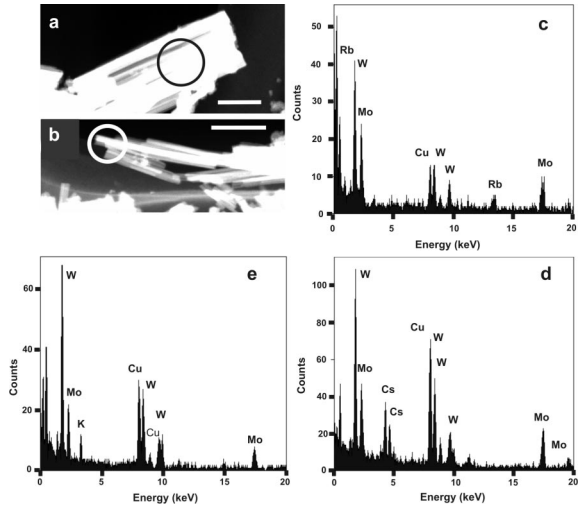

Figure 12. TEM images (scale bar = 100 nm) and EDX spot analyses of nanostructured K-W/Mo-HTB oxides (a,e), Rb-W/Mo-HTB oxides (b,c), and Cs-W/Mo oxides (d).

can be observed (Figure 10c,d). The products obtained in the MCl/AMT/$MoO_3 \cdot 2H_2O$ hydrothermal systems (M = Li−Rb) display the HTB structural motif. With CsCl, however, a small amount of pyrochlore (P-type) tungstate is obtained as a side product, and more detailed TEM characterizations are in progress. Previous studies in the CsCl/AMT hydrothermal system have shown that considerable optimization work is required to suppress the formation of P tungstates completely.[8]

Thus, the individual morphological trends of the alkali chlorides deteriorate when they are used in lower contents in the starting material: an initial M/(W/Mo)-ratio of 2.5:1 (M = Li−Cs) afforded strongly agglomerated spherical patterns of the alkali W/Mo-HTB oxides (cf. ESI for background analytical data).

The ratios of the metal atoms in the above-mentioned M-W/Mo oxides (M = Li−Cs) were analyzed with EDX spot analyses (Figure 12), verifying the simultaneous presence of W, Mo, and the respective alkali cation (K−Cs) in a single nanorod. The presence of Li and Na in the products was evidenced in terms of solid state NMR investigations (for details cf. section 3.5). In the Li-based systems, the W/Mo-ratio points to an approximately 1:1 distribution of both elements in the product. This also applies for most areas of the Na-containing W/Mo-HTB oxides, but specific parts of the sample display a slight excess of W. On the basis of the overall atomic percent of metallic cations, the products obtained with KCl contain approximately 15−18 atom % K, whereas the HTB framework is enriched in tungsten. RbCl is incorporated to a similar extent (17−20 atom %) into a less homogeneous HTB structure that exhibits a wider variation of the W/Mo-ratio. Finally, the Cs-W/Mo oxides contain around 20 atom % Cs in a Mo-enriched environment. Small amounts of stabilizing ammonium cations from the AMT starting material are also included in the HTB channels. The amount of NH_4^+ decreases consequently with the size of the alkali cation, as has been reported for the alkali HTB systems (for details cf. ESI).[8]

3.4.2. Influence of the Reaction Time and Temperature on the AMT/$MoO_3 \cdot 2H_2O$ Systems. As outlined above, the formation of alkali HTBs takes between 2 and 5 h, whereas the growth of W/Mo-HTB oxides is completed after approximately 1 h of reaction time. Therefore, the reaction in the MCl/AMT/$MoO_3 \cdot 2H_2O$ (M = Li−Cs) systems was stopped after 5 or 16 h, respectively, of treatment at 180 °C. After this time, the formation of alkali W/Mo-HTBs was finished in none of the systems. In the presence of LiCl, the formation of a mixed compound exhibiting the orthorhombic (O) tungstate structural motif precedes the conversion into the HTB phase, and the process takes more than 16 h. After 5 h, the Li−W/Mo oxides display an unusual growth pattern: A considerable amount of the sample is transformed into intersecting disk-shaped microcrystals that display further internal nanostructuring (Figure 13a,b). With NaCl, the formation of fibrous HTB already sets in after 5 h of reaction time (Figure 13c), but considerable amounts of the products still show a structure that is closely related to the hexagonal molybdate motif.[36] Here, the structural conversion is almost complete after 16 h. The addition of KCl to the AMT/$MoO_3 \cdot 2H_2O$ system leads to the formation of a compound with very low crystallinity after 5 h exhibiting a remote structural resemblance to the HTB target material. However, the characteristic spherical growth patterns are already present in the product (Figure 13d), together with hollow microcrystals decaying into nanorods. The crystallinity and purity of the compound is substantially improved after 16 h. RbCl, however, does not give rise to pure HTB formation after 5 h of treatment, and a complex mixture of phases is formed, including $Rb_2Mo_4O_{13}$, Rb-P-tungstate, and a phase displaying an orthorhombic mixed W/Mo-oxide motif. Nevertheless, considerable parts of the sample are already organized into spherical aggregates after 5 h (Figure 13e). After 16 h of treatment, this mixture contains increasing amounts of the HTB phase. On the other hand, the addition of CsCl favors the formation of a HTB/P-based mixed oxide product, and the XRD patterns recorded after 5 h and 16 h of reaction time show close resemblance to those obtained after 2 d of reaction time (cf. section 3.4.1). The same holds for the sample morphology after 5 h (Figure 13f).

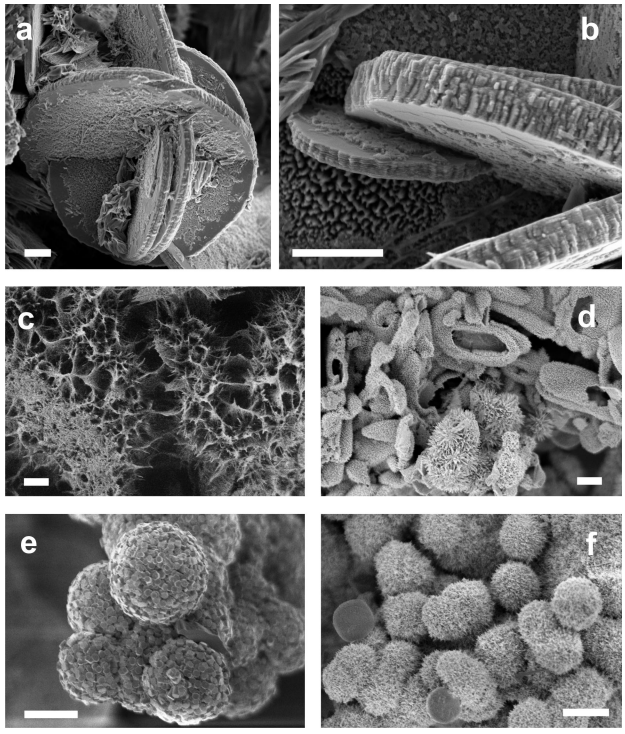

Figure 13. Representative SEM images of products formed after 5 h of hydrothermal treatment: (a,b) Li−W/Mo oxides (scale bar = 1 μm), (c) Na−W/Mo oxides, (d) K−W/Mo oxides, (e) Rb−W/Mo oxides, and (f) Cs−W/Mo oxides (c−f: scale bar = 2 μm).

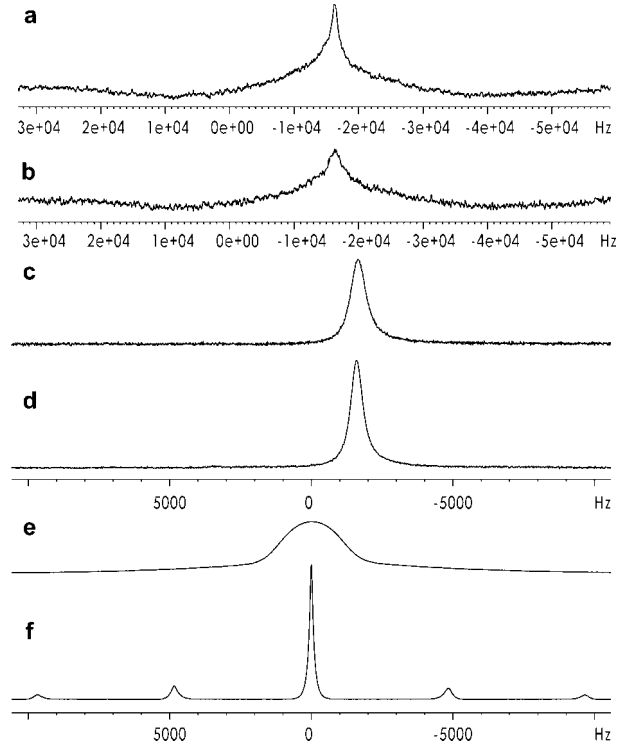

Figure 14. Solid state ^{133}Cs NMR spectra of Cs-W/Mo-HTB oxide (a) with MAS and (b) without MAS and solid state ^{23}Na NMR spectra of (c) Na-W/Mo HTB-oxide without MAS, (d) Na-W/Mo HTB-oxide with MAS, (e) NaCl without MAS, and (f) NaCl with MAS.

Furthermore, the formation of W/Mo-HTBs in the presence of alkali chlorides was investigated at 120 °C (cf. ESI). Whereas $(NH_4)_x(W,Mo)O_x$ HTB-rods with only very few remaining impurities are formed after 4 d of hydrothermal treatment at 100 °C from AMT/$MoO_3 \cdot 2H_2O$ starting materials,[9] the conversion into M-W/Mo HTB-nanostructured materials (M = Li−Cs) requires higher temperatures and/or longer reaction times. These results point to a very complex interaction of the alkali chlorides with the AMT/$MoO_3 \cdot 2H_2O$ hydrothermal system that requires detailed kinetic monitoring, and further investigations are in progress. Unlike the alkali HTB compounds that follow basically the same nucleation controlled mechanism, the formation pathways for alkali W/Mo-HTBs vary with the different MCl additives.

3.5. Solid State NMR Spectroscopy on Alkali W/Mo-HTB Oxides. Solid state NMR spectroscopy has been carried out in order to find evidence for mobility of the alkali metal sites within the transition metal oxides. All incorporated alkali metals (^{7}Li, ^{23}Na, ^{87}Rb, and ^{133}Cs) have half integer quadrupolar nuclear spins. Therefore, their solid state NMR spectra are dominated by the interaction of the quadrupolar moment with the electric field gradient. Chemical shift anisotropy and dipolar interactions are negligible in non-spherical symmetric environments. Furthermore, the central transition (±1/2) of non-integer spins is not affected by first order quadrupolar interactions, and MAS need only remove the much smaller second order effects leading to line narrowing by approximately a factor of four in rigid systems of low symmetry. The non-central transitions of half integer quadrupolar spins are suppressed as a result of first order quadrupolar interactions and have therefore no influence onto the line shape.[38]

In our NMR studies the MAS line width dependency of the incorporated alkali chloride and comparison with the pure rigid chloride served as a probe for mobility. Line widths in the typical range of some kHz with high sensitivity to MAS are an indication for rigid systems. In contrast, narrow lines below 1 kHz with low sensitivity to MAS are evidence for diffusion, which averages the quadrupolar interactions in the solid environment within the NMR time scale, in the rapid mode leading to line shapes even as in the liquid phase. Furthermore, ^{7}Li T_1 time measurements were carried out for the lithiated systems, applying the inversion recovery method.[39] The obtained T_1 data served as an additional, sensitive probe for the dynamic behavior of the appropriate lithium sites. Generally, quadrupolar T_1 relaxation is more efficient in dynamic systems with low symmetry, compared with rigid, symmetric systems, due to time-dependent spin lattice interactions, which occur in fluctual environments.[40]

Cs-W/Mo-HTB oxide shows a broad ^{133}Cs line (3.1 kHz) at 5 kHz MAS, −240 ppm shifted relatively to CsCl (Figure 14a, b). Without MAS the line width increases up to 5.8 kHz, being in the typical range of a static system with lower symmetry as in pure CsCl, where the line width is 76 Hz at 5 kHz MAS and 840 Hz in the static rotor. Also the large chemical shift difference to pure CsCl indicates the

(38) Fyfe, C. A. *Solid State NMR for Chemists*; Guelph: Ontario, Canada, 1983.
(39) Cowan, B. *Nuclear Magnetic Resonance and Relaxation*; Cambridge University Press: New York, 1997.
(40) Abragam, A. *Principles of Nuclear Magnetism*, Clarendon Press, Oxford, 1986.

absence of isolated CsCl units and is evidence for the incorporation of Cs into the W/Mo oxide lattice.

In contrast to pure NaCl the ^{23}Na resonance of the Na-W/Mo-HTB oxide (Figure 14c, d) is just slightly affected by MAS (510 Hz vs 660 Hz with and without MAS), being additionally much sharper as in the case of NaCl without MAS (660 Hz vs 2.6 kHz). That is in good agreement with the mobility of sodium which causes averaging effects leading to a fourfold sharper line, compared with the NaCl reference (Figure 14e, f). The chemical shift difference of 12 ppm relative to NaCl is not as significant as in the case of Cs relative to CsCl. Nevertheless, the line shape differences of Na-W/Mo-HTB oxide and pure NaCl (510 Hz vs. 160 Hz) at 5 kHz MAS show that the sodium environment in Na-W/Mo-HTB oxide is of lower symmetry, and therefore, no NaCl lattice is present.

Comparison of the ^{7}Li signals of Li-W/Mo-HTB oxide and Li-HTB tungstate suggests a higher lithium mobility in the latter one, where the line width without MAS amounts to 230 Hz in contrast to 5.8 kHz in Li-W/Mo-HTB oxide (Figure 15). In contrast to the sodium and cesium species, the NMR spectra of the lithiated compounds are influenced by chemical shift anisotropy (csa) effects rather than by quadrupolar interactions. Therefore, broad rotation side band patterns are observed under MAS conditions. This is evidence for a quasi-spherical symmetry with small electric field gradients at the lithium sites, resulting in just small quadrupolar interactions which are insignificant with respect to the csa effects. The presence of rotation side bands under MAS conditions not only for Li-W/Mo-HTB oxide but also in the case of Li-HTB tungstate indicates for the latter that there is rather a hindered lithium reorientation instead of free diffusion which would completely wipe out csa effects.

Li-W/Mo-HTB and Li-HTB tungstate show narrow ^{7}Li line widths (<70 Hz) under MAS conditions and two lithium sites with a chemical shift difference of 1.8 ppm could be distinguished for Li-HTB tungstate. The sharper line at lower field shows a narrow rotation side band pattern in contrast to the much broader high field signal with its large rotation side band extension. These differences are due to different environmental symmetries and site mobilities, as shown with ^{7}Li T_1 time measurements. The sharp low field signal of Li-HTB tungstate exhibits a T_1 time of just 469 ms, which is some orders of magnitude smaller than that one of ^{7}Li in pure LiCl (449 s). In contrast, the broad high field component of Li-HTB tungstate ranges with a T_1 time of 12.1 s between the values of pure LiCl and the Li-HTB tungstate component in the fast exchange mode. In the case of Li-W/Mo-HTB the ^{7}Li T_1 time amounts to 481 ms, which is comparable with the value of Li-HTB tungstate in the fast mode. This suggests a lower symmetry of the Li-W/Mo-HTB site which compensates the low lithium mobility and gives rise to a T_1 value, which is as short as the one of Li-HTB tungstate. Although ^{87}Rb has a high NMR sensitivity and a nuclear quadrupolar moment comparable with ^{23}Na and is therefore easy to detect, attempts to observe it in the WMo oxide framework were not successful. Under MAS conditions the RuCl reference showed a ^{87}Rb line shape pattern similar to that of NaCl already after four scans, but the spectrum of Rb−W/Mo-HTB oxide did not reveal any ^{87}Rb resonance even after 80 000 scans. This may be due to a tight fixation of rubidium in a low symmetric environment, leading to strong quadrupolar couplings causing line widths which exceed the limits of the NMR facility that was used. Isolated RbCl units do obviously not exist in the framework, because they should lead to an intense line pattern similar to pure RbCl.

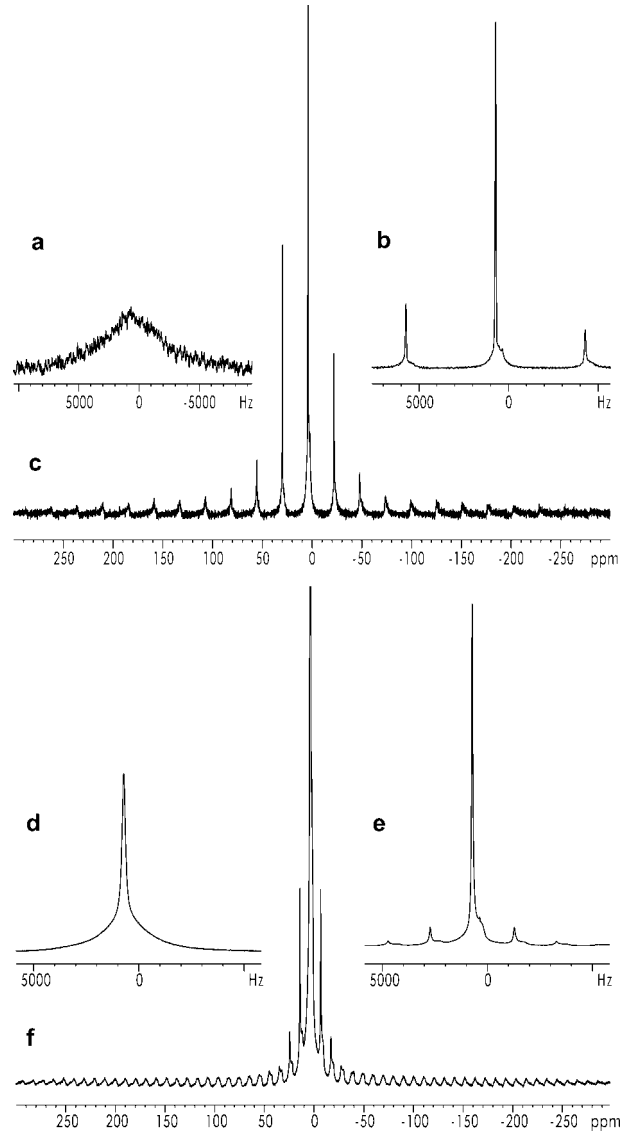

Figure 15. Solid state ^{7}Li NMR spectra of Li−W/Mo-HTB oxide (a) without MAS and (b,c) with MAS compared to solid state ^{7}Li NMR spectra of Li-HTB oxide (d) without MAS and (e,f) with MAS.

4. Discussion

Mixed nanoscale W/Mo-HTB oxides are accessible from AMT and $MoO_3 \cdot 2H_2O$ in a one-step hydrothermal reaction within approximately 1 h of reaction time at 180 °C. In situ EDXRD studies revealed that the kinetics of W/Mo-HTB nanorod growth is slower than that observed for the formation of MoO_3 fibers but faster than the growth process of nanostructured tungstates. Therefore, the slower growing tungstate component of the hydrothermal system determines both the nucleation-controlled formation mechanism and the overall reaction kinetics.[7,8] As a result, anisotropic W/Mo-

HTB oxides are obtained that are intermediate with respect to both the aspect ratio and the growth velocity of the binary Mo- and W-oxide nanomaterials. Other than in the binary systems, a hexagonal intermediate phase ($(NH_4)_{0.94}H_{3.3}Mo_{5.3}O_{18}$) could be identified in the course of the in situ EDXRD investigations. These results point out that the "construction" of ternary nanoparticles with a specific phase and morphology from binary hydrothermal systems is in principle possible. However, the underlying reaction mechanism may be different, and therefore each hydrothermal system must be studied individually. The present results furthermore indicate that much more information is required before the combination of hydrothermal processes and the general application of synthetic principles can be employed as a true "design" approach towards nanostructured materials. This holds especially for the complex redox and structural chemistry of ternary systems containing transition metal oxides, as has been illustrated in a recent in situ study on the formation of bismuth molybdate catalysts:[41] Even though in situ analyses provide the most valuable mechanistic insights, the optimization of materials is still a challenging interplay of established synthetic principles and concrete parameter optimizations in a given system. Furthermore, the hydrothermal formation of W/Mo-HTB oxides can be steered through the use of alkali chlorides as additives.[42] As has been observed for the formation of nanoscopic alkali HTBs, the individual alkali cations exhibit different morphological profiles:[8] whereas the addition of LiCl and NaCl directs the W/Mo-HTB oxides into fibrous structures, KCl as an additive induces an arrangement of these nanofibers into spherical patterns. This tendency is intensified with RbCl and CsCl, thereby resulting in a hierarchical organization of nanorods on three levels into microspheres. Among the hydrothermal reaction parameters, the type and concentration of the alkali additive exerts the most pronounced influence on the resulting morphology, followed by the reaction temperature and the reaction time. More detailed investigations concerning the effect of time and temperature on the phase of the product unraveled that the formation of mixed alkali W/Mo-HTB oxides displays different kinetics from the additive-free hydrothermal system. Further kinetic investigations are therefore in progress to shed light on the complex relations between cation incorporation, morphology control and the resulting growth kinetics. The preliminary results indicate that the presence of alkali cations further complicates the formation mechanisms of the resulting nanostructured W/Mo-HTB oxides: The individual cations display different kinetic profiles, and—other than in our previous studies—they also seem to change in the reaction mechanism. While the formation of hierarchical nanopatterns, for example, in the recently investigated $BaWO_4$ system,[43] can easily be classified on the basis of electron microscopy studies and other ex situ data as "oriented aggregation mechanism" with nucleation control, it takes considerably more effort to assign all intermediates and steps occurring in the formation process. The present results are a step towards such understanding, but the precise interaction of the different alkali cations with the planes of the different growing mixed W/Mo-oxide intermediates probably requires additional calculation methods. However, this effort is worthwhile to fully exploit the numerous applications of W/Mo materials in catalysis, sensor technology, and the construction of smart electrochromic materials. Especially for the production of nanostructured catalysts that benefit from the synergistic interaction of the two transition metal oxides, information about the thermal stability of the W/Mo-HTB framework and its follow-up reactions in different reactions is of key importance. Complementary in situ XRD and EXAFS techniques provide an excellent opportunity to monitor the onset of structural changes in nanoscale W/Mo-HTB oxides and their subsequent transformation into other nanomaterials in oxidizing and reducing atmospheres. In the O_2/He atmosphere, the mixed oxide material can be handled up to 390 °C without major structural changes, and a monoclinic structural motif is formed at higher temperatures. The thermal resilience is even higher in an H_2/He environment: Above 500 °C, the gradual formation of a nanostructured mixed W/Mo-metal sets in. Fourier transformed EXAFS data allowed monitoring these gradual structural changes individually for the local structure around the different absorber atoms before the net structural alterations are evident from the XRD patterns. This provides very detailed information for the thermal treatment and synthetic use of mixed W/Mo-HTBs.

As additive substances are key morphological tools in nanomaterials synthesis, their interaction with the structure of the target material needs to be studied in detail. In the case of alkali W/Mo-HTBs, solid state NMR spectroscopy illustrates that the interaction of the different intercalated alkali cations with the host W/Mo-channel structure influences not only the external morphology but also the cationic mobility within the channel system. Whereas the small Li^+ cations can occupy two sites with different environments and mobilities, the sodium cations display significant mobility only on the larger site. Consequently, Cs^+ ions are highly stabilizing yet less mobile. Interestingly, the substitution of W by Mo in the HTB channel framework also affects the mobility of the cations, as has been demonstrated comparing Li-W/Mo HTB oxides with their Mo-free analogues.

5. Conclusion

This study presents a multidisciplinary investigation of the hydrothermal kinetics, morphochemistry, and follow-up treatment of nanostructured W/Mo-HTB oxides. It demonstrates how preparative processes and analytical methods applied on the binary oxide systems can be extended upon the complex task of the controlled synthesis of ternary nanomaterials. On the preparative level, the use of readily available ionic additives opens up a wide spectrum of nanoscale morphologies. In situ EDXRD methods have proven to be a powerful tool to track down an intermediate compound in the nucleation-controlled formation of mixed W/Mo-HTBs. Concerning the follow-up treatment of the W/Mo-oxide nanomaterials in different atmospheres, a

(41) Beale, A.M.; Le, M. T.; Hoste, S.; Sankar, G. *Solid State Sci.* **2005**, *7*, 1141.
(42) Michailovski, A.; Krumeich, F.; Patzke, G. R. *Helv. Chim. Acta* **2004**, *87*, 1029.
(43) Luo, Y.; Tu, Y.; Yu, B.; Liu, J.; Li, J.; Jia, Z. *Mater. Lett.* **2007**, *61*, 5250.

combination of in situ EXAFS and in situ XRD is required to keep track of the complex structural transformations. The results are currently applied on the development of W/Mo-HTB-based catalysts.

The complex interplay between the internal W/Mo substitution in the hexagonal channel structure, the external morphological influence of the additive cation, and its mobility in the resulting mixed nanomaterials is furthermore investigated with the help of solid state NMR spectroscopy. All in all, alkali W/Mo-HTB compounds are excellent model systems for deriving structure-morphology relationships that are essential for the future design of nanomaterials and the results yield some rules of thumb for the synthesis of nanoparticles with a special shape and size. Further investigations on different oxidic systems are required to show whether some general rules can be formulated allowing a better control of the size, shape, and morphology of the nanosized materials.

Acknowledgment. We thank the Swiss-Norwegian beamlines at ESRF for providing beamtime for the in situ EXAFS/XRD measurements. H. Emmerich and W. van Beek (SNBL) are acknowledged for their kind support during the experiments. We gratefully acknowledge HASYLAB (DESY, Hamburg, Germany) for providing beamtime at beamline F3 for in situ EDXRD experiments. We thank Prof. Dr. Reinhard Nesper (Laboratory of Inorganic Chemistry, ETH Zurich) for the support of this work. The authors acknowledge support of the Electron Microscopy ETH Zurich, EMEZ. We thank Dr. Frank Krumeich, EMEZ, for STEM and EDX analyses. We are grateful to Heinz Spring, Institute of Inorganic Chemistry, University of Zurich, for elemental analyses. Financial support by the Swiss National Science Foundation (SNF Professorship PP002-114711/1 and MaNEP - Materials with Novel Electronic Properties) and by the University of Zurich is gratefully acknowledged.

Supporting Information Available: In situ XANES/EXAFS spectra of W/Mo-HTB oxide, elemental analyses concerning the ammonium content of alkali W/Mo-HTB oxides, preparative details of the hydrothermal preparation of alkali W/Mo HTBs (SEM images and tables), and additional EDX spot analyses of nanostructured alkali W/Mo HTBs (PDF). This material is available free of charge via the Internet at http://pubs.acs.org.

CM7028036